Biochimica et Biophysica Acta 1838 (2014) 968–977

Contents lists available at ScienceDirect

Biochimica et Biophysica Acta

journal homepage: www.elsevier.com/locate/bbamem

riDOM, a cell penetrating peptide. Interaction with phospholipid bilayers

Gabriela Québatte [a], Eric Kitas [b], Joachim Seelig [a,*]

[a] Biozentrum, University of Basel, Div. of Biophysical Chemistry, Klingelbergstrasse 50/70, CH-4056 Basel, Switzerland
[b] F. Hoffmann-La Roche Ltd., Pharma Research and Early Development Discovery Chemistry, Grenzacherstrasse 124, CH-4070 Basel, Switzerland

ARTICLE INFO

Article history:
Received 10 September 2013
Received in revised form 15 October 2013
Accepted 21 October 2013
Available online 1 November 2013

Keywords:
Cell penetrating peptide
Transfection
Peptide–membrane interaction
Pore formation
Melittin
Thermodynamic

ABSTRACT

Melittin is an amphipathic peptide which has received much attention as a model peptide for peptide–membrane interactions. It is however not suited as a transfection agent due to its cytolytic and toxicological effects. Retro-inverso-melittin, when covalently linked to the lipid 1,2-dioleoyl-*sn*-glycero-3-phosphoethanolamine (riDOM), eliminates these shortcomings. The interaction of riDOM with phospholipid membranes was investigated with circular dichroism (CD) spectroscopy, dynamic light scattering, ζ-potential measurements, and high-sensitivity isothermal titration calorimetry. riDOM forms cationic nanoparticles with a diameter of ~13 nm which are well soluble in water and bind with high affinity to DNA and lipid membranes. When dissolved in bilayer membranes, riDOM nanoparticles dissociate and form transient pores. riDOM-induced membrane leakiness is however much reduced compared to that of authentic melittin. The secondary structure of the ri-melittin is not changed when riDOM is transferred from water to the membrane and displays a large fraction of β-structure. The ^{31}P NMR spectrum of the nanoparticle is however transformed into a typical bilayer spectrum. The Gibbs free energy of riDOM binding to bilayer membranes is −8.0 to −10.0 kcal/mol which corresponds to the partition energy of just one fatty acyl chain. Half of the hydrophobic surface of the riDOM lipid extension with its 2 oleic acyl chains is therefore involved in a lipid–peptide interaction. This packing arrangement guarantees a good solubility of riDOM both in the aqueous and in the membrane phase. The membrane binding enthalpy is small and riDOM binding is thus entropy-driven.

1. Introduction

Melittin, an amphipathic peptide and the main component of the venom of the honey bee *Apis mellifera*, is probably the most widely studied membrane-interacting peptide. It possesses a net positive charge but easily inserts into lipid membranes [1–5]. Cationic melittin also binds to DNA with a high affinity by electrostatic interactions with the anionic phosphate backbone [6]. However the melittin/DNA complex does not mediate transfection and the complex is toxic caused probably by lysis of the cell membrane [7–9].

In order to reduce toxic effects and to improve both stability and transfection efficiency of melittin/DNA complexes different approaches have been used. Melittin analogs, PEI–melittin, and polylysine–melittin conjugates have been synthesized. They mediate efficient transfection, but their lytic activity is still high [7,8,10]. Other systems such as poly-melittin peptides and polylysine–melittin–dimethylmaleic acid conjugates exhibit reduced toxicity of melittin and high gene expression levels [10,11].

An alternative method to create a stable and efficient gene delivery system is the conjugation of a peptide to a lipid moiety [12–15]. Dioleoylmelittin (DOM) is one of such hybrid molecules [13]. It has been synthesized by covalent binding of a lipid, dioleoylphosphatidylethanolamine-N-[3-(2-pyridyldithio)propionate], to an analog of melittin, [Cys^1]melittin, in which the N-terminal glycine is replaced by cysteine. Electron microscopy of DOM solutions using uranyl acetate staining suggests spherical structures with diameters between 5 and 10 nm. When DOM is added to plasmid DNA it forms homogeneous particles with a diameter of ~170 to 250 nm depending on the DNA/DOM ratio.

DOM is an efficient transfection agent [13]. However, even though DOM has a lower hemolytic activity than melittin, it is still toxic and not stable. Retro-inverso dioleoylmelittin (riDOM) is identical to DOM except that all L-amino acid residues are replaced by the corresponding D-isomers and the amino acid sequence of the peptide is reversed (cf. Table 1) [16]. As riDOM is composed of D-amino acids, it can be expected to have a higher resistance to enzymatic degradation, and thus to show a better in vivo performance [16–18]. riDOM mediates efficient transfection and when mixed with cationic polymeric compounds a synergistic enhancement of transfection is observed [16]. The net positive charge of riDOM facilitates the binding to DNA. We have shown by dynamic light scattering and solid state ^{31}P NMR that riDOM in solution forms stable nanoparticles, composed of ~250 riDOM molecules, with a diameter of ~13 nm and a ζ-potential of 22 mV [6]. It binds to anionic polymers such as DNA or heparan sulfate with a high affinity [6]. During the binding process the riDOM nanoparticles are dissolved and larger DNA/riDOM or heparan sulfate complexes are formed. The physical–

* Corresponding author. Tel.: +41 61 267 2190; fax: +41 61 267 2189.
E-mail addresses: gabriela.quebatte@unibas.ch (G. Québatte), eric_a.kitas@roche.com (E. Kitas), joachim.seelig@unibas.ch (J. Seelig).

0005-2736/$ – see front matter © 2013 Published by Elsevier B.V.
http://dx.doi.org/10.1016/j.bbamem.2013.10.017

Table 1
Chemical structure of riDOM. In red — positively charged amino acids.

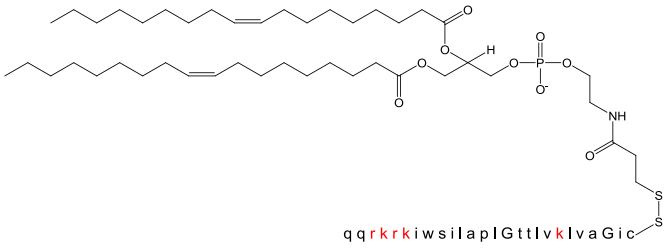

chemical properties of riDOM are thus different from other cell penetrating peptides or poly-cations [19–25].

Efficient internalization of transfecting agents can be due to insertion into and perturbation of lipid membranes as shown for cell penetrating peptides such as transportan and pep-1 [26,27]. Alternatively, the uptake of cationic molecules can be mediated by anionic glycosaminoglycans (GAGs), which are present on almost all cell surfaces [24,28–31]. We were therefore interested to characterize the mechanism of interaction and the binding affinities of riDOM with lipid membranes as it could shed light on the transfection mechanism.

We have used high-sensitivity isothermal titration calorimetry (ITC) to obtain a complete thermodynamic characterization of riDOM binding to lipid bilayers composed of 1-palmitoyl-2-oleoyl-*sn*-glycero-3-phosphatidylcholine (POPC) and 1-palmitoyl-2-oleoyl-*sn*-glycero-3-phosphatidylglycerol (POPG). Dynamic light scattering measurements were used to characterize size and ζ-potential of riDOM/lipid complexes. Structural properties of the peptide alone and upon association with lipid membranes were followed by circular dichroism (CD) spectroscopy. In addition the structure of the phospholipid bilayer in the presence of riDOM was studied with solid-state phosphorus-31 nuclear magnetic resonance spectroscopy (^{31}P NMR) and with a dye efflux assay.

2. Materials and methods

2.1. Materials

Synthetic melittin was from Bachem (Bubendorf, Switzerland). Retro-inverso dioleoylmelittin (riDOM) (MW: 3723 Da) was from F. Hoffman-La Roche Ltd. (Basel, Switzerland). The chemical structure of riDOM is given in Table 1. 1-Palmitoyl-2-oleoyl-*sn*-glycero-3-phosphocholine (POPC) and 1-palmitoyl-2-oleoyl-*sn*-glycero-3-phospho-glycerol (POPG) were purchased from Avanti Polar Lipids Inc. (Alabaster, AL). 8-Aminonaphtalene-1,3,6-trisulfonic acid, disodium salt (ANTS) was from Molecular Probes (Eugene, Oregon, USA). *N*,*N*′-*p*-xylylenebis(pyridinium bromide) (DPX) was from Sigma Aldrich (Buchs, Switzerland).

All other chemicals were of analytical or reagent grade. Tris buffer (10 or 25 mM tris(hydroxymethyl)aminoethane, pH 7.4) was prepared with 18 MΩ water obtained from a NANOpure A filtration system. NaCl concentrations were typically 50 mM if not specified otherwise. The samples were degassed immediately before use.

2.2. Preparation of lipid vesicles

A defined amount of POPC was dried from a stock solution in chloroform with a gentle stream of nitrogen followed by a high vacuum overnight. For POPC/POPG mixed membranes, the amount of POPC was weighed and mixed with a defined volume of POPG stock solution in chloroform to yield a POPC/POPG molar ratio of 75/25 (mol/mol). The solvent was removed as above, and the lipid film was exposed to high vacuum overnight and weighed again. For POPC/POPG/PEG mixtures the POPC/POPG lipid film was mixed with a defined volume of PEG stock solution in chloroform to yield a POPC/POPG/PEG molar ratio of 74/25/1 (mol/mol/mol). The solvent was removed and the lipid weighed again. The lipid film was resuspended in buffer and vortexed, leading to multilamellar vesicles (MLVs) with c_L^0 ~10 mM. Large unilamellar vesicles (LUVs) with a diameter of d ~100 nm were prepared by extrusion of the MLV suspension. After five consecutive freeze–thaw cycles, MLVs were extruded 15 times through a polycarbonate membrane with a pore diameter of 100 nm (Whatman, Clifton, NJ). Small unilamellar vesicles (SUVs) with a diatmeter of 25–30 nm were prepared by sonication of the MLV suspension using a titanium tip ultrasonicator (Branson Sonifier, Danbury, CT) until an almost clear solution was obtained (40 min). Metal debris from the sonicator tip was removed by centrifugation for 4 min in an Eppendorf 5415 C benchtop centrifuge (Vaudaux-Eppendorf AG, Schonenbuch, Switzerland).

2.3. ^{31}P solid-state NMR

Solid-state ^{31}P NMR experiments were performed on a Bruker Avance 400 MHz spectrometer (Bruker AXS, Karlsruhe, Germany). 8–10 mg of POPC/POPG (75/25 mol/mol) were dispersed in 150–500 μL buffer (25 mM Tris, 50 mM NaCl, pH 7.4) containing different amounts of riDOM. The samples were vortexed, freeze-thawed and vortexed again. The pure riDOM was measured at a concentration of 8.63 mg dissolved in 180 μL Tris buffer.

Spectra were recorded at 162 MHz using a pulse-acquire sequence with broadband proton decoupling (WALTZ-16) and a recycle delay of 5 s. The excitation pulse length was 4.5 μs and 20,000 free induction decays (FID) were accumulated. In the measurements of riDOM in the absence of lipids a recycle delay of 1 s, and an excitation pulse of 4.5 μs were used and 50,000 FID were accumulated.

The FID were exponentially multiplied prior to Fourier transformation corresponding to a 100 Hz line broadening.

2.4. Isothermal titration calorimetry

A MicroCal VP-ITC calorimeter (MicroCal, Northampton, MA) was used. Lipid–into-peptide titrations were performed by injecting 5–12 μL aliquots of lipid suspension at c_L^0 ~10 mM into the calorimeter cell (V_{cell} = 1.4037 mL) containing melittin or riDOM, at concentrations of ~10–30 μM. Peptide–into-lipid titrations were performed by injecting 10 μL aliquots of a peptide solution (c_{riDOM} ~200 μM) into a lipid SUV suspension (concentration ~10 mM).

The heats of dilution were determined in control titrations by injecting the lipid suspension or the peptide solution into buffer. The heats of dilution were small and were included in the final analysis. Raw data were processed using the Origin software provided with the instrument. If not specified otherwise all measurements were performed in 25 mM Tris, 50 mM NaCl, pH 7.4.

2.5. Circular dichroism spectroscopy

CD measurements of riDOM were made with and without POPC/POPG (75/25 mol/mol) small unilamellar vesicles (SUV) in buffer (25 mM Tris, 50 mM NaF, pH 7.4) with a Chirascan CD spectrometer (Applied Photophysics Ltd., Leatherhead, U.K.).

A quartz cuvette with a 1 mm path length was used. All spectra were corrected by subtracting the buffer or buffer with lipid baseline. The percentage of peptide secondary structure was estimated from a computer simulation based on the reference spectra obtained by Reed and Reed [32].

2.6. Measurement of vesicle size and ζ-potential with dynamic light scattering (DLS)

The size and ζ-potential of riDOM nanoparticles in the absence and the presence of different amounts of POPC/POPG (75/25 mol/mol) SUVs were measured with a Zetasizer Nano ZS (Malvern Instrument Ltd., Worcestershire, UK). Samples were prepared in Tris buffer (25 mM Tris, 50 mM NaCl, pH 7.4) and measured at room temperature.

2.7. Release of ANTS/DPX from lipid vesicles

ANTS/DPX release measurements were performed on a Jasco FP-6500 Spectrofluorometer (Jasco Inc., Easton, MD, USA). A lipid film (POPC or POPC/POPG (75/25 mol/mol)) was prepared as described above, and Tris buffer containing 12.5 mM ANTS and 45 mM DPX was added. After five freeze–thaw cycles, MLVs were extruded 20 times through a polycarbonate membrane with a pore diameter of 100 nm (Whatman, Clifton, NJ). Unentrapped dye was removed from the large unilamellar vesicles (LUVs) by gel filtration on a Sephadex G75 column equilibrated with Tris buffer.

The dye-containing LUVs were diluted in a 5 mm quartz cuvette to yield $c_L^0 = 1.75$ mM in Tris buffer. riDOM was added by injection of a stock solution under rapid mixing. The release of dye from vesicles was monitored using an excitation wavelength of 360 nm and an emission wavelength of 518 nm. The intensity was monitored for 6–7 min. The intensity value for 100% lysis (maximum leakage) was obtained by injection of 25 μL of a 5% Triton X-100 solution. The measurements were performed at different peptide concentrations to produce different peptide-to-lipid molar ratios.

2.8. Binding model

The analysis of the ITC experiments proceeds in two steps [33]. (i) The injection of phospholipid vesicles into a melittin or riDOM solution produces a series of heat peaks, h_i, which decrease to zero when all peptide in the calorimeter cell is lipid-bound. The h_is are used to derive the binding isotherm, $X_b = f(c_{eq})$, which describes the molar amount of bound peptide as a function of the free peptide, c_{eq}. X_b is the extent of binding, defined by $X_b = c_b/c_L^0$, where c_b is the molar concentration of bound peptide and c_L^0 is the total lipid concentration. It is assumed that melittin and riDOM rapidly translocate across the bilayer membrane. c_{eq} is the equilibrium concentration of free peptide. The concentrations of free and bound peptide add up to the total protein concentration, c_P^0.

$$c_b + c_{eq} = X_b c_L^0 + c_{eq} = c_P^0 \quad (1)$$

X_b can be measured directly in the ITC experiment and the binding isotherm X_b vs. c_{eq} can be constructed without applying a specific binding model [33]. (ii) The binding of a cationic peptide to a neutral or charged membrane is driven by both chemical adsorption (characterized by a binding constant K_0) and electrostatic attraction/repulsion (characterized by surface potential ψ and surface charge density σ). A negatively charged membrane will exert a strong attractive force for a cationic peptide. However, if the peptide binds beyond electroneutrality (strong chemical adsorption) the interaction becomes repulsive as the now positive surface charge of the membrane will repel ions of like charge. For neutral membranes the binding of the cationic peptide immediately generates an electrostatic repulsion. The surface concentration of peptide, c_M, directly above the plane of binding is different from its equilibrium concentration, c_{eq}, in bulk solution. c_M can be calculated for a given surface potential ψ with the Boltzmann equation.

$$c_M = c_{eq} e^{-z_p F_0 \psi / RT} \quad (2)$$

where z_p is the effective peptide charge, F_0 the Faraday constant and RT the thermal energy. The peptide binding to the lipid membrane can then be described by a surface partition equilibrium

$$X_b = K_0 c_M = K_0 c_{eq} e^{-z_p \psi F_0 / RT}. \quad (3)$$

In this model, "binding" is defined as a nonspecific adsorption of peptide to the lipid membrane. As peptide is bound to the membrane surface, it changes the membrane surface charge density, σ, and, in turn, the surface potential. The connection between σ and the surface potential ψ is given by the Gouy–Chapman theory [34,35]. We have used this model, that is, the combination of a surface partition equilibrium with the Gouy–Chapman theory to successfully describe the interaction of melittin [2,36,37] and other peptides [38–42] with neutral and charged membranes. The model demonstrates that the binding constant K_0 is independent of electrostatic effects and is constant over a large concentration range. As a further result the analysis yields the effective charge, z_p, of the peptide.

It should also be noted that the model as applied here includes Na^+ binding to the phosphoglycerol headgroup by a Langmuir adsorption isotherm [38]. The Na^+ ion binding constant is $K_{Na^+} = 0.6\,M^{-1}$.

3. Results

3.1. riDOM conformation with and without lipids as determined with circular dichroism spectroscopy

Fig. 1 compares the CD spectra of retro-inverso [cys[1]]melittin (ri-mel-SH; no lipid extension) and riDOM in buffer with and without lipid vesicles. ri-mel-SH in buffer adopts a random coil conformation (60–70% random coil). Upon addition of phospholipid vesicles the conformation changes to ~60% α-helix, a behavior very similar to that of authentic melittin [3,5]. Compared to melittin, the CD spectra of ri-mel-SH are mirror-imaged at the x-axis as the molecule is composed of D-amino acids only. A different CD-spectrum is obtained for riDOM. The peptide conformation of riDOM in solution is characterized by a large contribution of β-structure (31% β-structure, 30% α-helix, 39% random coil) [6]. This structure is almost temperature-independent. In the present study POPC/POPG (75/25 mol/mol) vesicles (SUVs) were added to the riDOM solution. The CD spectrum of riDOM (Fig. 1) was measured in excess lipid at $c_L^0 : c_P^0 = 28.5$; nevertheless, the spectrum is virtually identical to that of riDOM without lipid. At this lipid-to-riDOM ratio a homogeneous lipid bilayer is observed with ^{31}P NMR spectroscopy (cf. below). riDOM appears to be completely immersed in the lipid bilayer. Nevertheless, the CD spectrum of riDOM does not display the high α-helix content observed for ri-mel-SH measured under the same conditions.

3.2. Size effects and ζ-potential measurements of riDOM–phospholipid interactions

riDOM is not soluble in monomeric form but aggregates into nanoparticles of well-defined size (d ~13 ± 1 nm) composed of 220–

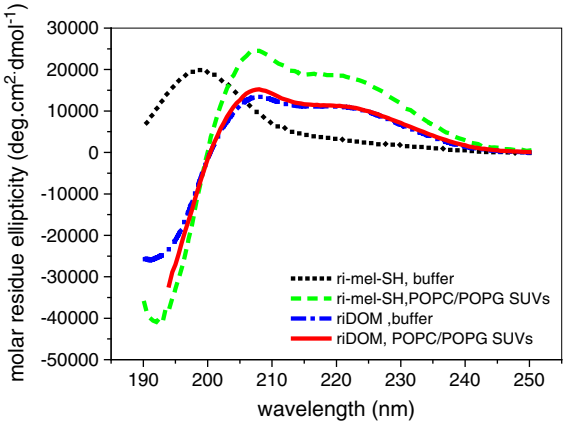

Fig. 1. Circular dichroism spectra of ri-melittin-SH and riDOM in buffer and with lipid vesicles. (•••, short dot) ri-mel-SH at a concentration of 19.21 μM in buffer, no lipid; (--, short dash) ri-mel-SH with POPC/POPG (75/25 mol/mol) SUVs $c_L^0 : c_P^0 = 70$; (— . —, dash-dot line) riDOM in buffer, no lipid; (—, solid line) riDOM at a concentration of 42 μM with 1.13 mM POPC/POPG (75/25 mol/mol) small unilamellar vesicles, $c_L^0 : c_P^0 = 26.9$. All measurements in 25 mM Tris, 50 mM NaF, pH 7.2 at 30 °C.

270 molecules [6]. Using dynamic light scattering (DLS) we studied the interaction of riDOM nanoparticles with small unilamellar vesicles (SUVs) composed of POPC/POPG (75/25 mol/mol). In the absence of riDOM, the vesicle diameter was 24.6 nm and the ζ-potential −29 mV (25 m Tris, 50 mM NaCl, pH 7.4, 30 °C). The calculated Henry correction factor for 25 nm SUVs was 1.26 [43]. The corrected ζ-potential of the POPC/POPG SUVs was thus −34.5 mV.

In Fig. 2 the vesicle size and the corresponding ζ-potential are plotted vs. the riDOM-to-lipid molar ratio. In a first experiment, the measuring cell contained SUVs (POPC/POPG (75/25 mol/mol), $c_L^0 = 0.84$ mM) and riDOM nanoparticles were added. The initial vesicle size of ~25 nm remained nearly constant up to $c_P^0 : c_L^0 = 0.016$ (Fig. 2A). At these low riDOM concentrations the nanoparticles were integrated into the lipid bilayer with little change in the dimensions of the SUVs. Upon further addition of riDOM the vesicle diameter increased to d ~35 nm at a $c_P^0 : c_L^0 = 0.03$, with DLS still indicating a monomodal vesicle distribution. Beyond this threshold the particle size increased rapidly to a maximum of 65–70 nm (accounting for 70% of total volume) at $c_P^0 : c_L^0 = 0.15$–0.2. In addition, much larger particles with d ~300 nm (~30% total volume) were observed.

In a second experiment the sample cell contained the riDOM nanoparticles (diameter 12.2 nm; $c_P^0 = 39.3$ μM) and POPC/POPG SUVs were added. This initially produced large phospholipid–riDOM particles with a diameter of d ~73 nm at $c_P^0 : c_L^0 = 0.16$. Upon further addition of lipid, the size of the particles decreased gradually to reach d ~30 nm at $c_P^0 : c_L^0 = 0.02$. Fig. 2A displays both experiments and shows a good agreement between the two modes of titration. It demonstrates that the riDOM-induced vesicle aggregation is a dynamic equilibrium which can be reversed at sufficiently high riDOM concentrations.

The increase in aggregation size further demonstrates that riDOM has little or no detergent-like properties. An interesting contrasting example is the 20-residue tandem dimer $(LRKLRKRLLR)_2$ to which two palmitoyl chains were linked [44]. This amphipathic molecule is similar to riDOM as it also carries 2 fatty acyl chains. However, its peptide extension is highly charged and the molecule dissolves lipid bilayers already at low concentrations.

Fig. 2B displays the variation of the ζ-potential as a function of the riDOM-to-lipid ratio. Data of both types of titration (lipid-into-riDOM, riDOM-into-lipid) are included and again good agreement is observed. The ζ-potential of the pure lipid vesicles was negative due to its POPG content. Addition of the cationic riDOM nanoparticles led to an almost linear increase in the ζ-potential with the increasing $c_P^0 : c_L^0$ ratio. The ζ-potential became zero at $c_P^0 : c_L^0$ ~0.11–0.125. As the POPG content was 25% of total lipid, the $c_P^0 : c_{POPG}^0$ ratio at electroneutrality ($\zeta = 0$ mV) was ~0.45–0.5, provided all POPG was available to riDOM. As POPG carries the electric charge $z = -1$, the average riDOM charge must be z_p ~2–2.2 to produce electroneutrality. The effective riDOM charge is clearly smaller than the maximum riDOM charge of $z_p = 5$. This result is however consistent with riDOM binding data to DNA and heparan sulfate where effective riDOM charges of 1.7 (DNA(bp)) and 1.8 (heparan sulfate) were deduced [6]. It is further in agreement with the more precise ITC data discussed below where z_p is in the range of $1.5 \leq z_p \leq 2.0$ at 30 °C.

3.3. ^{31}P NMR studies of riDOM–phospholipid interactions

The molecular structure of riDOM upon insertion into bilayer membranes was investigated with ^{31}P NMR. Solid state ^{31}P NMR spectroscopy is a quantitative technique to study the structure and dynamics of both lipid model membranes and biological membranes. Characteristic spectra of different shapes are observed for bilayers, hexagonal phases, and micelles [45]. For studies of membranes, ^{31}P NMR spectroscopy usually requires multilamellar lipid dispersions. Small vesicles or micellar structures produce sharp lines as rapid vesicle rotation or micellar fluctuations average out the chemical shielding anisotropy of the ^{31}P nucleus. In the present experiments, a lipid film was produced on the surface of a glass tube and a small amount of a concentrated riDOM solution was added. The mixture was then vortexed to

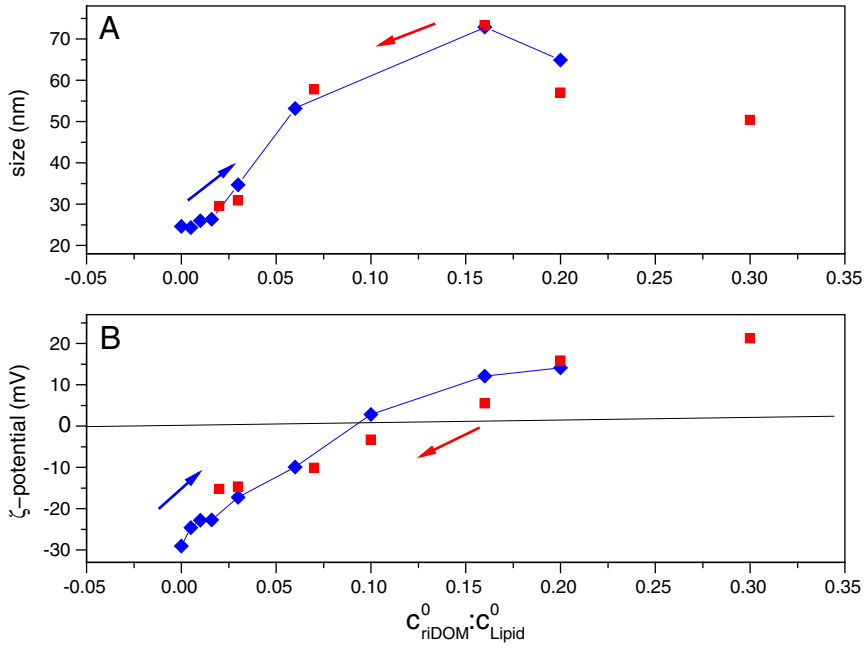

Fig. 2. Binding of riDOM to lipid vesicles. (A) Size measurements with dynamic light scattering. POPC/POPG (75/25 mol/mol) small unilamellar vesicles (SUVs) binding to riDOM. 30 °C; buffer: 25 mM Tris, 50 mM NaCl. (♦) Different amounts of a riDOM stock solution ($c_{riDOM} = 187.2$ μM) were added to a suspension of phospholipid vesicles ($c_L^0 = 0.84$ mM); (■) inverse experiment. Lipid vesicles ($c_L^0 = 8.38$ mM) were added to a riDOM solution ($c_{riDOM} = 39.3$ μM). The arrows indicate the direction of the concentration changes of the two types of titration. (B) ζ-Potential measurements. Interaction of riDOM nanoparticles with POPC/POPG (75/25 mol/mol) small unilamellar vesicles. (♦) riDOM solution into a SUV suspension; (■) SUVs injected into a riDOM solution. The arrows indicate the direction of the concentration changes.

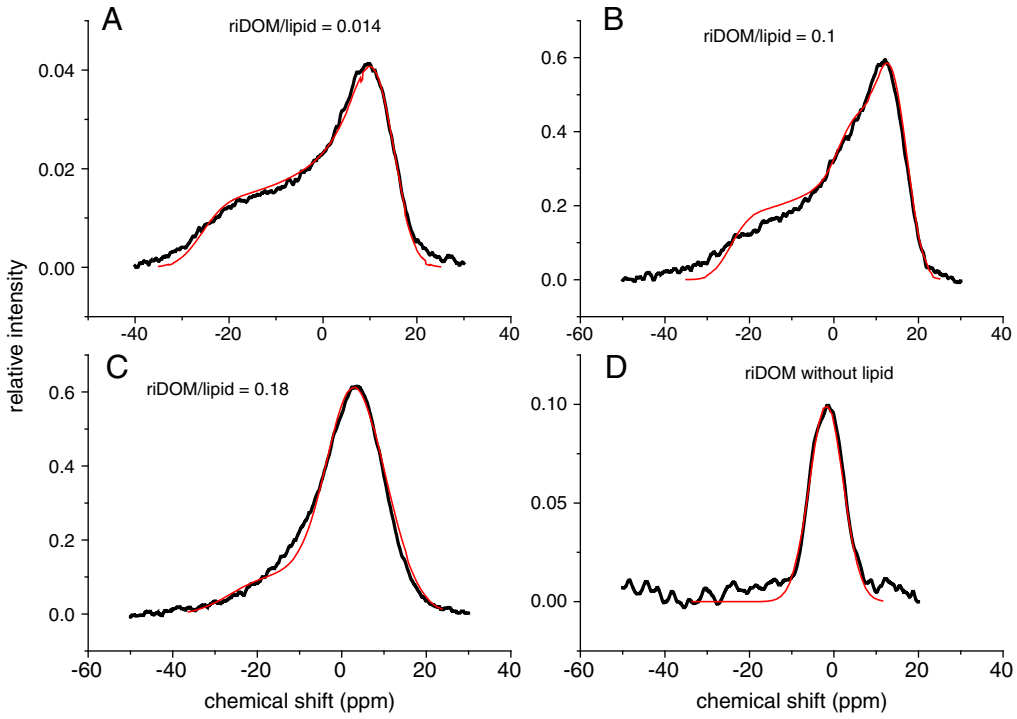

Fig. 3. ^{31}P NMR spectra of multilamellar phospholipid dispersions containing different concentrations of riDOM. Phospholipid composition: POPC/POPG 75/25 (mol/mol). Buffer composition 25 mM Tris, 50 mM NaCl, pH 7.4. 8–10 mg of phospholipid with different amounts of riDOM were suspended in 150–200 μL buffer. (A) riDOM/phospholipid molar ratio r = 0.014. (B) r = 0.1. (C) r = 0.18. (D) Pure riDOM particles. 8.63 mg riDOM dissolved in 180 μL buffer. riDOM particle diameter ~13 nm as determined by dynamic light scattering.

homogeneity. Representative spectra obtained at different riDOM-to-phospholipid ratios are displayed in Fig. 3. In Fig. 3A (B) the $c_P^0 : c_L^0$ ratio is 0.014 (0.1). The ^{31}P NMR spectra in Fig. 3A, B are typical for a random distribution of bilayer domains ("powder-type spectrum") and can be simulated by very similar parameters, that is, a chemical shielding anisotropy of $\Delta\sigma = -37$ to -39 ppm and an intrinsic line broadening of 3.5–4 ppm. This result is quite unexpected as the bilayers are composed of three different components, namely 2 phospholipids (POPC, POPG) and a lipopeptide (riDOM), the latter also containing a ^{31}P-atom. In the POPC–POPG–riDOM membrane the differences between the individual molecules are however smoothed out and even the non-bilayer spectrum of pure riDOM nanoparticles (Fig. 3D) is transformed into a bilayer spectrum. Without knowledge of the chemical composition, the ^{31}P NMR spectra in Fig. 3A, B of the riDOM-containing preparations could be mistaken for one-component phospholipid bilayers. The ^{31}P NMR spectra thus provide evidence that the riDOM nanoparticles are dissolved in the phospholipid bilayer. It should be noted that the incorporation of riDOM leaves the peptide secondary structure unchanged but increases the permeability of the lipid membrane (cf. below).

Increasing the $c_P^0 : c_L^0$ ratio to 0.18 led to the ^{31}P NMR spectrum shown in Fig. 3C. It can be simulated by a superposition of a bilayer spectrum with a chemical shielding anisotropy of $\Delta\sigma = -39$ ppm and the spectrum of pure riDOM nanoparticles with an isotropic line width of -4 ppm (Fig. 3D). At sufficiently high riDOM concentrations not all riDOM nanoparticles are dissolved but some fraction is incorporated in intact form into the phospholipid bilayer.

3.4. Efflux measurements

Large unilamellar vesicles (~100 nm diameter) were prepared in buffer (25 mM Tris, 50 mM NaCl, pH 7.4) in the presence of 12.5 mM ANTS/45 mM DPX. External dye was removed by gel filtration over Sephadex. The lipid concentration was typically 1.75 mM. riDOM was added at different concentrations and the dye efflux was measured as a function of time. After 6 min, maximum dye release, F_∞, was established by dissolving the vesicles with Triton X-100. Fig. 4A shows the outflow of dye measured by the increase in fluorescence for several riDOM concentrations. Increasing the riDOM concentration increases both the extent and the speed of dye release. The data in Fig. 4A can be normalized to yield the fraction F(t) of dye retained in the LUVs:

$$F(t) = \frac{F_\infty - F(t)}{F_\infty - F_0}. \quad (4)$$

F(t) is the experimental fluorescence intensity at time t, and F_∞ the fluorescence intensity after vesicles disruption. F_0 is the background fluorescence at the beginning of the experiment. The normalized efflux curves calculated from the data in Fig. 4A are displayed in Fig. 4B. They can be described quantitatively by a 2-exponential decay of the form

$$f(t) = A_0 + A_1 \cdot e^{-t/\tau_1} + A_2 e^{-t/\tau_2} \quad (5)$$

The amplitudes A_0, A_1 and A_2 denote the fraction of lipid vesicles which show either no dye release (A_0) or dye release (A_1, A_2), the latter with time constants τ_1 or τ_2, respectively. The fit parameters for POPC and POPC/POPG (75/25 mol/mol) LUVs are summarized in Table 2.

Inspection of Table 2 reveals a systematic variation of all parameters with the riDOM:lipid molar ratio. At $c_P^0 : c_L^0 \leq 0.006$ a large fraction of vesicles showed no efflux at all. The population of non-leaking vesicles (A_0) decreased linearly with increasing riDOM concentration and was replaced by two vesicle populations with long (τ_1 ~300–120 s) and short (τ_2 ~40–4 s) relaxation times. Fig. 4C shows that for POPC/POPG (POPC) LUVs the leakage was 100% at $c_P^0 : c_L^0 > 0.02$ (0.01) and that POPC/POPG LUVs are more tightly sealed than POPC LUVs. Increasing the riDOM concentration not only increases the fraction of dye-permeable vesicles but also decreases the relaxation times (cf. Table 2). At the highest riDOM-to-lipid ratio $c_P^0 : c_L^0 = 0.06$ the dye efflux can be described by a single exponential with a short (~4 s) relaxation time.

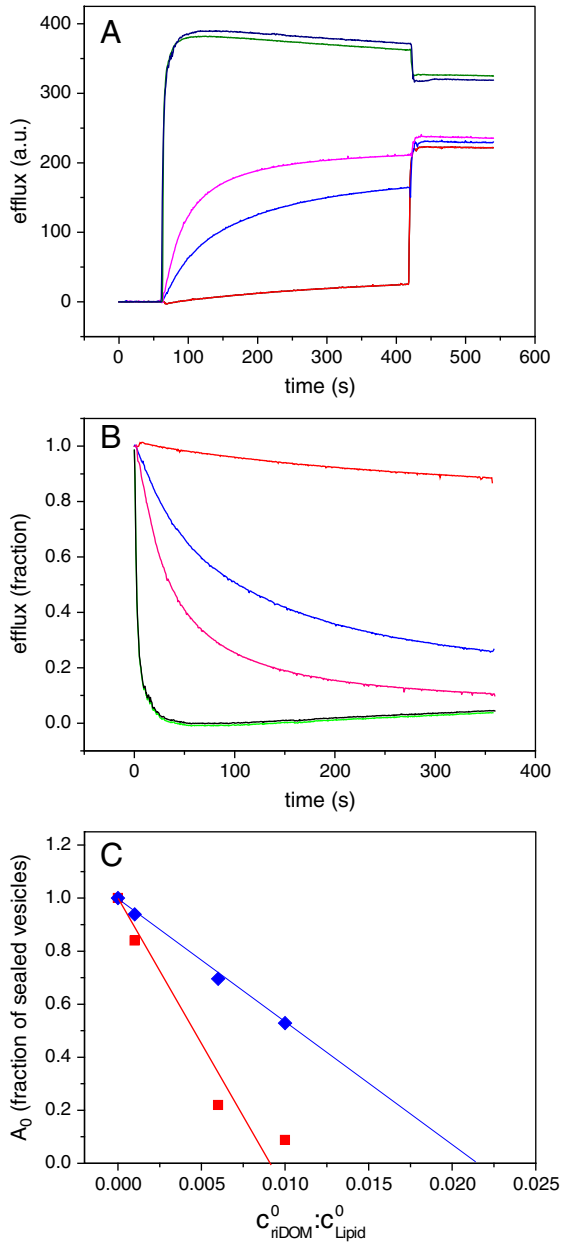

Fig. 4. Dye efflux from lipid vesicles induced by riDOM. Increasing concentrations of riDOM were added to POPC/POPG (75/25 mol/mol) large unilamellar vesicles (LUVs). The LUVs were loaded with the fluorophore-quencher pair 12.5 mM ANTS/45 mM DPX in buffer (25 mM Tris, 50 mM NaCl, pH 7.4). The lipid concentration was 1.75 mM. (A) Efflux curve, fluorescence intensity F(t) versus time. riDOM/lipid ratios from bottom-to-top are 0.001, 0.006, 0.01, and 0.06 (2 experiments). (B) Dye retained in LUVs according to $(F_\infty - F(t)) / (F_\infty - F_0)$. Color code as in (A). (C) Fraction of non-leaking lipid vesicles. A_0 is the normalized amplitude of lipid vesicles which in the bi-exponential analysis do not show dye leakage. (♦) POPC/POPG (75/25 mol/mol) LUVs; (■) POPC LUVs. Mixed POPC/POPG LUVs are less sensitive to riDOM induced dye efflux than POPC LUVs.

3.5. Interaction of riDOM and authentic melittin with bilayer membranes measured with isothermal titration calorimetry (ITC)

The riDOM–phospholipid thermodynamics was investigated with ITC. Experiments were performed as a function of temperature and phospholipid composition with POPC and POPC/POPG (75/25 mol/mol) SUVs. The size of the vesicles was measured with dynamic light scattering.

Fig. 5 shows a typical titration experiment at 10 °C. The calorimeter cell (V_{cell} = 1.4037 mL) contained riDOM (30.8 μM) in buffer. Each heat flow peak in Fig. 5A corresponds to the injection of 10 μL POPC SUVs at a phospholipid concentration of c_L^0 = 8.0 mM, producing an exothermic response, h_i. The reaction comes to an end when all riDOM is bound to the injected lipid. The molar heat of reaction is then given by $\sum h_i/(c_p^0 \cdot V_{cell})$ where c_P^0 is the riDOM concentration in the calorimeter cell. For the example given in Fig. 5 the reaction enthalpy is $\Delta H_{riDOM}^0 = -6.0$ kcal/mol (at 10 °C).

Table 2
Dye efflux data analyzed according to $f(t) = A_0 + A_1 e^{-t/\tau_1} + A_2 e^{-t/\tau_2}$.

Lipid	riDOM/Lipid	A_0	A_1	τ_1 (s)	A_2	τ_2 (s)
POPC	0.001	0.83	0.17	296 ± 3	–	–
	0.006	0.22	0.50	174 ± 3	0.29	38
	0.01	0.09	0.36	114	0.55	25
	0.06	0.02 ± 0.02	–	–	0.95 ± 0.05	3.8 ± 0.3
POPC/POPG 75/25 mol/mol	0.001	0.94	0.03	137	0.03	9.6
	0.006	0.7	0.13	120	0.11	8.2
	0.01	0.53	0.18	135	0.26	9.0
	0.06	–	–	–	1.0	4.3 ± 1.5

Fig. 6A summarizes the temperature dependence of ΔH_{riDOM}^0 for the various systems investigated. The reaction enthalpies were always small and exothermic and became less negative with increasing temperature. The molar heat capacity change as referred to riDOM was positive with ΔC_P^0 = 262 cal/molK for POPC SUVs and 90 cal/molK for POPC/POPG SUVs. Also included in Fig. 6A are the enthalpies measured for authentic melittin binding to POPC/POPG SUVs. The solid line is the linear regression analysis of the latter experiments yielding a slope of ΔC_P^0 = 298 cal/molK. The positive heat capacity changes in all three experiments are quite unexpected as hydrophobic interactions are characterized by a negative ΔC_P^0. Indeed, melittin binding to 100 nm vesicles (LUVs) of the same composition led to $\Delta C_P^0 = -200$ to −400 cal/molK [2]. We have therefore measured the binding enthalpy of riDOM to POPC/POPG LUVs by titration of riDOM into a LUV suspension. In the temperature interval 20–40 °C the molar heat capacity change is also negative with $\Delta C_P^0 = -85$ cal/molK.

The variation of the heats of reaction, h_i, can be used to deduce the binding isotherm. Fig. 5B shows the analysis of the experimental data in Fig. 5A in terms of the surface partition model (solid line). The binding constant for the data shown in Fig. 5 was $K_0 = 8 \times 10^4$ M^{-1}. Fig. 6B then displays the temperature dependence of the binding constant, K_0, for POPC and POPC/POPG (75/25 mol/mol) SUVs. The error in evaluating K_0 is mainly caused by the small reaction enthalpies, ΔH_{riDOM}^0. Also included in Fig. 6B are the binding constants of authentic melittin recorded for POPC/POPG (75/25 mol/mol) SUVs. Despite the missing lipid extension they are similar to those of riDOM and fall in the range of 3×10^4 M^{-1} to 6×10^4 M^{-1} for temperatures between 50 °C and 10 °C. We have previously determined the binding constant of melittin to POPC/POPG SUVs with CD spectroscopy [37]. The binding constant K_0 was $(4.5 \pm 0.6) \times 10^4$ M^{-1} in agreement with the analysis presented here. A numerical summary of all thermodynamic data is presented in Table 3.

The solid line in Fig. 6B represents the theoretical temperature dependence of melittin binding to POPC/POPG SUVs calculated with the van't Hoff equation and the temperature dependent enthalpy in Fig. 6A (linear regression ΔH_{mel}^0 (kcal/mol) = 0.298x − 11.59; x = in °C). The binding affinity exhibits a minimum at 38 °C as the reaction enthalpy becomes zero. Fig. 6B shows close numerical agreement between the binding constants K_0 of authentic melittin and riDOM, independent of the lipid composition.

Inspection of Table 3 shows that the effective riDOM charge, leading to a consistent evaluation of all binding curves, is independent of the lipid composition. Its average value $z_{riDOM} = 1.63 \pm 0.27$ is clearly below the nominal charge of ri-melittin of z = +5 but in agreement with the ζ-potential measurements and previous studies with DNA and heparan sulfate [6]. The effective charge of authentic melittin in the present analysis is however larger with $z_{mel} = 4$, in agreement with an earlier study with POPC/POPG LUVs [2].

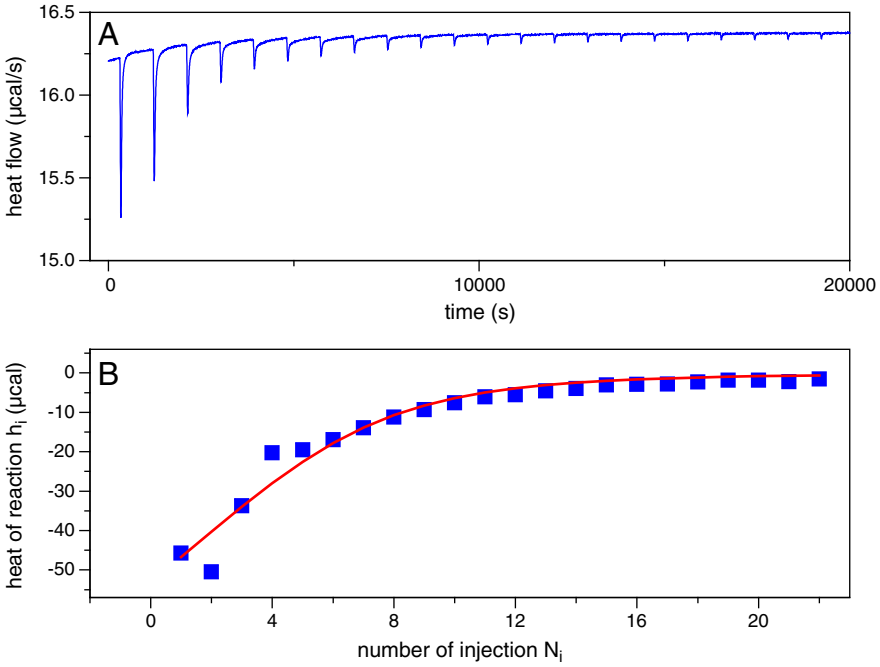

Fig. 5. Isothermal titration calorimetry. Interaction of riDOM with POPC unilamellar vesicles. A riDOM solution (30.8 µM) was titrated with POPC SUVs (8 mM) in buffer (25 mM Tris, 50 mM NaCl, pH 7.4) at 10 °C. (A) Heat flow. Injection of 10 µL aliquots ($c_L^0 = 8$ mM). (B) Heats of reaction, h_i. (■) Experimental data obtained by integration of heat flow. Solid line: membrane partition model combined with electrostatic repulsion calculated with the Gouy–Chapman theory. Effective charge of riDOM z = 1.6; partition constant $K_0 = 8 \times 10^4\ M^{-1}$, partition enthalpy $\Delta H_{riDOM} = -6.0$ kcal. It was assumed that riDOM can translocate rapidly across the membrane.

4. Discussion

riDOM is an efficient transfection agent, melittin however is not. Specific toxicological effects aside, the physical—chemical results obtained here provide insight into the different action mechanisms of the two molecules.

The interaction of authentic melittin with lipid membranes has been studied extensively with different methods. ITC data have been published for 100 nm vesicles (LUVs) [2] but not for 30 nm vesicles (SUVs). ITC measurements on melittin binding to SUVs are therefore included as a control in the present study.

4.1. riDOM nanoparticles with and without phospholipids

Authentic melittin in solution is mainly random coil at low µM concentrations. It forms α-helical tetramers at concentrations ≥100 µM

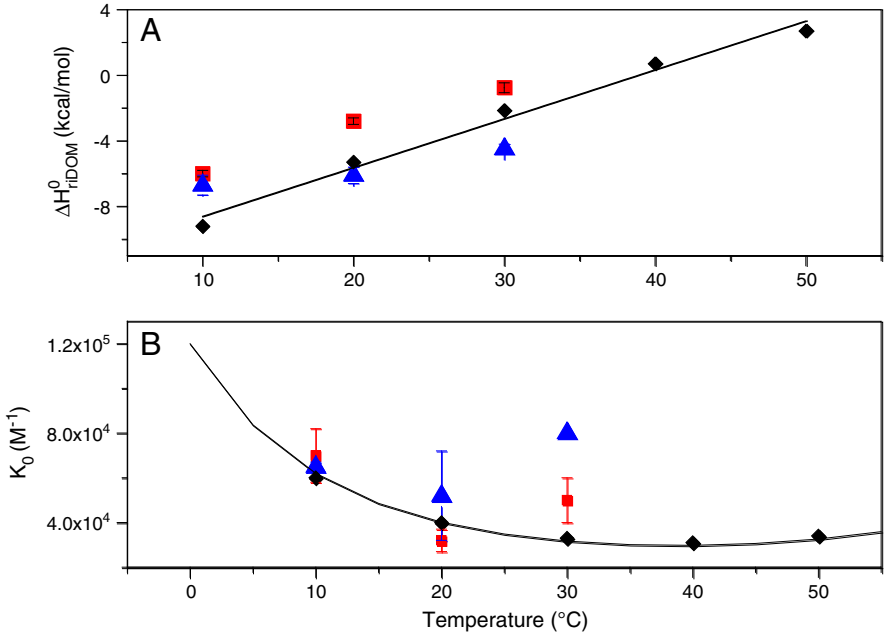

Fig. 6. Thermodynamic parameters for the binding of riDOM and authentic melittin to bilayer membranes. (A) Binding enthalpy ΔH^0. (B) Binding constant K_0. (♦) Authentic melittin and (▲) riDOM binding to POPC/POPG (75/25 mol/mol) SUVs. (■) riDOM binding to POPC SUVs. The solid line in (B) corresponds to the theoretical temperature dependence of authentic melittin. It was calculated with the van't Hoff equation using the enthalpy data of (A).

Table 3
Thermodynamic parameters. Binding of riDOM and melittin to POPC/POPG (75/25 mol/mol) bilayers.[a]

Peptide	Lipid	Temp °C	z_{riDOM}	ΔH_{riDOM} kcal/mol	K_0 M^{-1}
riDOM	POPC SUVs	10	1.6 ± 0.1	−6.0 ± 0.1	(7.0 ± 1.2) × 10^4
		20	1.00	−2.8 ± 0.1	(3.2 ± 0.5) × 10^4
		30	1.6 ± 0.3	−0.76	5.0 × 10^4
	POPC–POPG SUVs 75/25 mol/mol	10[b]	1.9 ± 0.3	−5.9 ± 0.5	(5.5 ± 0.6) × 10^5
		10	1.9 ± 0.3	−6.7 ± 0.6	(6.5 ± 0.2) × 10^4
		20	1.60	−6.1 ± 0.5	(5.2 ± 2.0) × 10^4
		30	1.50	−4.5 ± 0.3	8 × 10^4
Melittin	POPC–POPG SUVs 75/25 mol/mol	10	4	−9.2	6.0 × 10^4
		20	4	−5.3	4.0 × 10^4
		30	4	−2.15	3.3 × 10^4
		40	4	0.7	3.1 × 10^4
		50	4	2.7	3.4 × 10^4

[a] If not otherwise stated all measurements in 25 mM Tris, 50 mM NaCl, pH 7.4.
[b] 25 mM Tris, 25 mM NaCl, pH 7.4.

[46–48]. Upon binding to lipid membranes melittin adopts an α-helical conformation [5]. The membrane-bound melittin also tends to form aggregates which have been characterized by isothermal titration calorimetry and spectroscopic methods [2,4]. The melittin aggregates comprise 6–20 monomers with a low stability constant of ~20–40 M^{-1} [2].

The lipopeptide riDOM shows a different behavior as it forms stable nanoparticles in solution with a ^{31}P NMR spectrum typical for isotropic tumbling of a large particle [6]. The secondary structure of ri-mel-SH without lipid extension is 73% random coil in buffer, changing to 60% α-helix upon addition of phospholipid SUVs. The β-sheet content of ri-mel-SH is only 17% in buffer and 8% in the bilayer membrane. In contrast, riDOM shows almost equal contributions of α-helix (30%), β-sheet (31%) and random coil (39%). The addition of lipid induces only small changes in the riDOM secondary structure (α-helix 30%, β-sheet 35%, and random coil 35%).

We can use the secondary structure for a rough estimate of the riDOM length. Using 0.15 nm for an α-helical segment and 0.35 nm for a β-sheet segment we calculate the riDOM (i) α-helix in buffer (lipid) as ~1.0 nm (1.2 nm), (ii) β-sheet in buffer (lipid) as 3.5 nm (3.0 nm), (iii) lipid moiety when linearly extended as ~3.5 nm and (iv) linker region as ~0.8 nm.

For a spherical particle with a diameter of 13.4 nm the length of an individual riDOM molecule cannot exceed 6.7 nm. Based on hydrophobicity considerations, the lipid moiety of riDOM must form the inner core of the sphere while the polar N-terminus (amino acids qqkrkr of ri-mel-SH) (cf. Table 1) is exposed to the aqueous phase. With some flexing motion of the lipid chains, the lipid moiety contributes ~2.9 nm to the particle radius. This leaves 3.8 nm as the maximum extension for peptide and linker moiety, which is clearly less than the estimated 5.3 nm for a linear alignment of α-helix, β-sheet and linker segments. Some folded conformation of the peptide moiety is therefore required to adjust to the space requirements in the nanoparticle. Upon addition of phospholipid membranes, the CD spectrum and hence the secondary structure of riDOM are essentially unchanged. In contrast, the ^{31}P NMR spectrum of riDOM changes from that of a slowly tumbling particle to a typical bilayer spectrum. This suggests that upon insertion into a bilayer membrane the spherical particle is flattened into a disk-like structure of about the thickness of the bilayer. The ri-melittin residues could form the inner core of the disk retaining their secondary structure through peptide–peptide interactions. This model explains (i) the intact bilayer structure as recorded by ^{31}P NMR and (ii) the simultaneous leakiness of the bilayer membrane as observed by dye efflux.

4.2. Efflux measurements

The action mechanism of many antibacterial peptides is based on their binding to the cell membrane and inducing membrane leakiness. Quantitative studies on the melittin-induced leakage of lipid vesicles have been performed by measuring the efflux of a self-quenching dye [49]. A graded dye efflux was observed as characterized by two distinct relaxation steps with relaxation times of ~20 s and ~200 s which were assigned to pore formation. The pore formation rate itself increased in proportion to the amount of membrane-bound melittin. Efflux occurred already in cases where 0.1–1% of the vesicle surface was covered with peptide. The number of melittin molecules forming a pore was estimated as low as 2–4.

It was also realized at the same time that the observed dye efflux was too slow if a stable pore was formed. Assuming a lipid vesicle with a diameter of 100 nm and a stable pore with a diameter of 4 nm the dye efflux should have been finished in a few milliseconds [50]. The rate determining step thus appeared not to be the efflux proper but the formation of the pore i.e. the association of several melittin molecules in the correct lateral position.

The dye efflux curves observed in this study also suggest the formation of transient pores through the association of several riDOM molecules. At low $c_P^0 : c_L^0$ ratios, pore formation is rare and many vesicles show no efflux at all. At higher concentrations, riDOM association leads to two types of pores, characterized by slow and fast relaxation times, respectively. The contribution of the fast process increases with riDOM concentration. The concentration dependence of the efflux curves requires a dissociation of riDOM nanoparticles in the bilayer membrane. The variation of the dye efflux relaxation times indicates the association of freely diffusing riDOM molecules into transient pores. Formation of long-lived, stable pores can be excluded as even the minimum relaxation time of ~2 s is still 2–3 orders of magnitude longer than the predicted efflux time of a stable pore.

A comparison with authentic melittin allows the following conclusions. (i) The riDOM induced membrane permeability is much reduced compared to melittin. A large fraction of vesicles remains sealed if riDOM is employed at low concentration. In transfection studies the concentration of free riDOM is so small that an injury of the cell membrane by inducing leakage can be excluded. (ii) Pore formation in the lipid model membrane requires a threshold concentration of riDOM. Two different types of pores appear to be formed, characterized by two relaxation times. This behavior is similar to authentic melittin but the relaxation times of riDOM are shorter than those of melittin. The lipid anchor of riDOM may force the covalently bound peptide into a membrane alignment more favorable for peptide–peptide association.

4.3. Thermodynamics of riDOM–membrane interaction

The binding of cationic riDOM or melittin to anionic membranes is initiated by the electrostatic attraction to the membrane surface, followed by chemical adsorption. The binding constant K_0 as derived with the model discussed above refers to the chemical adsorption step only. As the binding model eliminates electrostatic effects, K_0 should be identical for charged and non-charged membranes provided the membrane

properties are otherwise identical. This is indeed borne out experimentally comparing POPC and POPC/POPG SUVs (Table 3). The K_0 values of both membrane compositions are similar and range between 3×10^4 M^{-1} and 8×10^4 M^{-1}.

The free energy of binding can be calculated as $\Delta G^0 = -RT \ln (55.5\ K_0)$ and is in the range of −8.4 to −9.0 kcal/mol. The factor 55.5 is the molar concentration of water. As the concentration of riDOM in the membrane phase is given as mole fraction, the factor 55.5 converts the concentration in the aqueous phase to mole fraction as well.

riDOM partitioning into lipid bilayers may be compared with that of free fatty acids. The partition coefficient and the free energy of transfer of long-chain fatty acids from water to bilayer membranes have been measured [51,52]. For oleic acid a partition coefficient of 5×10^5 and a free energy change of −10.0 kcal have been reported. The partition coefficient was almost temperature independent.

For 1,2-dioleoyl-*sn*-glycero-3-phosphoethanolamine (DOPE) with 2 oleic acyl chains a free energy change twice as large (−20 kcal/mol) can be calculated for the transfer from water to the lipid membrane. Indeed, DOPE is virtually insoluble in water. However, the riDOM transfer free energy is only −8 to −10 kcal/mol. The hydrophobic surface area of DOPE thus appears to be divided into a DOPE–peptide interaction (50–60%) and a DOPE–bilayer interaction. The former exists already in the riDOM nanoparticles and is not changed upon insertion into the membrane as judged from the constancy of the CD spectra. The remaining hydrophobic area is equivalent to about 1 oleic acyl chain.

The binding constants, K_0, for authentic melittin are also in the range of 3×10^4 M^{-1} to 6×10^4 M^{-1} for SUVs (this work) and LUVs [2] and are thus similar to those of riDOM. The molecular origin of the free energy of insertion is however completely different. For melittin α-helix formation and α-helix insertion into the membrane are the driving forces. It has been estimated that α-helix formation accounts for at least 50% of the free energy of melittin membrane binding [2].

In spite of their similar binding constants K_0, authentic melittin and riDOM display large quantitative differences in their extent of binding to negatively charged membrane. This can be traced back to the different electric charges of the two molecules. Melittin with its effective charge $z = 4$ experiences a much stronger electrostatic attraction to the anionic POPC/POPG membrane than riDOM with $z = 1.6$–2.0. At identical melittin and riDOM concentrations in solution this generates a 20–40 times higher surface concentration of melittin compared to riDOM, generating a correspondingly higher insertion of melittin into the membrane. This potentiates the melittin-induced leakiness of membranes as the higher melittin concentration increases pore formation.

Inspection of Fig. 6 and Table 3 demonstrates that the reaction enthalpies of riDOM and melittin, ΔH^0, are close to zero at physiological temperatures. As the free energy is $\Delta G^0 \approx -8$ to −10 kcal/mol the membrane partition of riDOM and authentic melittin is determined exclusively by entropic contributions. riDOM undergoes no structural change upon insertion into the membrane and the structure of the lipid membrane is also unaffected. The molecular origin of the gain in entropy is therefore a release of hydration water as riDOM inserts into the membrane.

4.4. riDOM binding to DNA and heparan sulfate

The binding affinities of riDOM and melittin to lipid bilayers must be compared with those observed for DNA and sulfated glycosaminoglycans such as heparan sulfate (HS) [6]. riDOM is the vehicle to transport DNA across the cell membrane. HS may however interfere because riDOM could stick to sulfated glycosaminoglycans on the outer membrane surface. The microscopic binding constants of riDOM are 5×10^7 M^{-1} for DNA and 5×10^6 M^{-1} for HS. Even though lipid is much in excess, the riDOM:DNA complex will remain intact because of its high stability. This is further enhanced by the insolubility of DNA in a hydrophobic environment. As a working model it may be assumed that the riDOM:DNA complex translocates not as a single species but that several riDOM:DNA molecules aggregate into a pore with an inner riDOM–DNA core and an outer lipid mantle, the latter provided by the lipid extension of riDOM. The HS molecule can compete with the riDOM:DNA complex because of its large binding constant. An efficient transfection is thus achieved only if riDOM is applied at concentrations above the stoichiometric DNA:riDOM ratio in order to neutralize the sulfated glycosaminoglycans on the cell surface.

The packing density of the riDOM:DNA complex is also an important factor in membrane insertion and translocation. For riDOM the packing density is 1 riDOM:0.85 DNA(bp) and 1 riDOM:1 HS disaccharide unit whereas for melittin the ratios are less favorable with 1 mel:2 DNA(bp) and 1 mel:3 HS disaccharide units. The shielding of DNA by riDOM is distinctly more efficient than the shielding produced by melittin.

5. Conclusions

riDOM is an efficient transfection agent because it is well soluble in water but nevertheless binds with high affinity to DNA and lipid membranes. Pore formation and riDOM-induced membrane leakiness is much reduced compared to authentic melittin. The secondary structure of the riDOM peptide is not changed when riDOM is transferred from water to the membrane. In contrast, the change in the ^{31}P NMR spectrum demonstrates that riDOM via its DOPE extension becomes an integral part of the bilayer membrane. The free energy of insertion is however only half of the expected value for DOPE as part of the hydrophobic DOPE surface is involved in peptide interaction.

Acknowledgements

This work was supported by the Swiss National Science Foundation grant # 31003A-129701.

References

[1] E. Habermann, Bee and wasp venoms, Science 177 (1972) 314–322.
[2] G. Klocek, T. Schulthess, Y. Shai, J. Seelig, Thermodynamics of melittin binding to lipid bilayers. Aggregation and pore formation, Biochemistry 48 (2009) 2586–2596.
[3] G. Klocek, J. Seelig, Melittin interaction with sulfated cell surface sugars, Biochemistry 47 (2008) 2841–2849.
[4] M.T. Lee, W.C. Hung, F.Y. Chen, H.W. Huang, Mechanism and kinetics of pore formation in membranes by water-soluble amphipathic peptides, Proc. Natl. Acad. Sci. U. S. A. 105 (2008) 5087–5092.
[5] H. Vogel, Incorporation of melittin into phosphatidylcholine bilayers. Study of binding and conformational changes, FEBS Lett. 134 (1981) 37–42.
[6] G. Québatte, E. Kitas, J. Seelig, riDOM, a cell penetrating peptide. Interaction with DNA and heparan sulfate, J. Phys. Chem. B 117 (2013) 10807–10817.
[7] S. Boeckle, J. Fahrmeir, W. Roedl, M. Ogris, E. Wagner, Melittin analogs with high lytic activity at endosomal pH enhance transfection with purified targeted PEI polyplexes, J. Control. Release 112 (2006) 240–248.
[8] S. Boeckle, E. Wagner, M. Ogris, C- versus N-terminally linked melittin–polyethylenimine conjugates: the site of linkage strongly influences activity of DNA polyplexes, J. Gene Med. 7 (2005) 1335–1347.
[9] M. Ogris, R.C. Carlisle, T. Bettinger, L.W. Seymour, Melittin enables efficient vesicular escape and enhanced nuclear access of nonviral gene delivery vectors, J. Biol. Chem. 276 (2001) 47550–47555.
[10] M. Meyer, A. Zintchenko, M. Ogris, E. Wagner, A dimethylmaleic acid–melittin–polylysine conjugate with reduced toxicity, pH-triggered endosomolytic activity and enhanced gene transfer potential, J. Gene Med. 9 (2007) 797–805.
[11] C.P. Chen, J.S. Kim, E. Steenblock, D. Liu, K.G. Rice, Gene transfer with poly-melittin peptides, Bioconjug. Chem. 17 (2006) 1057–1062.
[12] J.Y. Legendre, A. Supersaxo, Short-chain phospholipids enhance amphipathic peptide-mediated gene transfer, Biochem. Biophys. Res. Commun. 217 (1995) 179–185.
[13] J.Y. Legendre, A. Trzeciak, B. Bohrmann, U. Deuschle, E. Kitas, A. Supersaxo, Dioleoylmelittin as a novel serum-insensitive reagent for efficient transfection of mammalian cells, Bioconjug. Chem. 8 (1997) 57–63.
[14] C.A. Prata, X.X. Zhang, D. Luo, T.J. McIntosh, P. Barthelemy, M.W. Grinstaff, Lipophilic peptides for gene delivery, Bioconjug. Chem. 19 (2008) 418–420.
[15] S. Zhang, Y. Zhao, B. Zhao, B. Wang, Hybrids of nonviral vectors for gene delivery, Bioconjug. Chem. 21 (2010) 1003–1009.
[16] E.J. Schlaeger, E.A. Kitas, A. Dorn, SEAP expression in transiently transfected mammalian cells grown in serum-free suspension culture, Cytotechnology 42 (2003) 47–55.
[17] M. Chorev, M. Goodman, Recent developments in retro peptides and proteins—an ongoing topochemical exploration, Trends Biotechnol. 13 (1995) 438–445.

[18] M.D. Fletcher, M.M. Campbell, Partially modified retro-inverso peptides: development, synthesis, and conformational behavior, Chem. Rev. 98 (1998) 763–796.
[19] D.J. Coles, A. Esposito, H.T. Chuah, I. Toth, The synthesis and characterization of lipophilic peptide-based carriers for gene delivery, Tetrahedron 66 (2010) 5435–5441.
[20] D.J. Coles, S. Yang, R.F. Minchin, I. Toth, The characterization of a novel dendritic system for gene delivery by isothermal titration calorimetry, Biopolymers 90 (2008) 651–654.
[21] D. Matulis, I. Rouzina, V.A. Bloomfield, Thermodynamics of cationic lipid binding to DNA and DNA condensation: roles of electrostatics and hydrophobicity, J. Am. Chem. Soc. 124 (2002) 7331–7342.
[22] E. Pozharski, R.C. MacDonald, Lipoplex thermodynamics: determination of DNA–cationic lipoid interaction energies, Biophys. J. 85 (2003) 3969–3978.
[23] A. Ziegler, J. Seelig, High affinity of the cell-penetrating peptide HIV-1 Tat-PTD for DNA, Biochemistry 46 (2007) 8138–8145.
[24] A. Ziegler, J. Seelig, Contributions of glycosaminoglycan binding and clustering to the biological uptake of the nonamphipathic cell-penetrating peptide WR9, Biochemistry 50 (2011) 4650–4664.
[25] T. Ehtezazi, U. Rungsardthong, S. Stolnik, Thermodynamic analysis of polycation–DNA interaction applying titration microcalorimetry, Langmuir 19 (2003) 9387–9394.
[26] K. Saar, M. Lindgren, M. Hansen, E. Eiriksdottir, Y. Jiang, K. Rosenthal-Aizman, M. Sassian, U. Langel, Cell-penetrating peptides: a comparative membrane toxicity study, Anal. Biochem. 345 (2005) 55–65.
[27] R. Sauder, J. Seelig, A. Ziegler, Thermodynamics of lipid interactions with cell-penetrating peptides, Methods Mol. Biol. 683 (2011) 129–155.
[28] S.M. Fuchs, R.T. Raines, Pathway for polyarginine entry into mammalian cells, Biochemistry 43 (2004) 2438–2444.
[29] M. Tyagi, M. Rusnati, M. Presta, M. Giacca, Internalization of HIV-1 tat requires cell surface heparan sulfate proteoglycans, J. Biol. Chem. 276 (2001) 3254–3261.
[30] S. Violini, V. Sharma, J.L. Prior, M. Dyszlewski, D. Piwnica-Worms, Evidence for a plasma membrane-mediated permeability barrier to Tat basic domain in well-differentiated epithelial cells: lack of correlation with heparan sulfate, Biochemistry 41 (2002) 12652–12661.
[31] A. Ziegler, P. Nervi, M. Durrenberger, J. Seelig, The cationic cell-penetrating peptide CPP(TAT) derived from the HIV-1 protein TAT is rapidly transported into living fibroblasts: optical, biophysical, and metabolic evidence, Biochemistry 44 (2005) 138–148.
[32] J. Reed, T.A. Reed, A set of constructed type spectra for the practical estimation of peptide secondary structure from circular dichroism, Anal. Biochem. 254 (1997) 36–40.
[33] J. Seelig, Titration calorimetry of lipid–peptide interactions, Biochim. Biophys. Acta 1331 (1997) 103–116.
[34] R. Aveyard, D.A. Haydon, An Introduction to the Principles of Surface Chemistry, Cambridge University Press, London, 1973.
[35] S.A. McLaughlin, Electrostatic potentials at membrane–solution interfaces, Curr. Top. Membr. Transp. 9 (1977) 71–144.
[36] E. Kuchinka, J. Seelig, Interaction of melittin with phosphatidylcholine membranes. Binding isotherm and lipid head-group conformation, Biochemistry 28 (1989) 4216–4221.
[37] G. Beschiaschvili, J. Seelig, Melittin binding to mixed phosphatidylglycerol/phosphatidylcholine membranes, Biochemistry 29 (1990) 52–58.
[38] J. Seelig, S. Nebel, P. Ganz, C. Bruns, Electrostatic and nonpolar peptide-membrane interactions. Lipid binding and functional properties of somatostatin analogues of charge $z = +1$ to $z = +3$, Biochemistry 32 (1993) 9714–9721.
[39] M.R. Wenk, J. Seelig, Magainin 2 amide interaction with lipid membranes: calorimetric detection of peptide binding and pore formation, Biochemistry 37 (1998) 3909–3916.
[40] T. Wieprecht, O. Apostolov, M. Beyermann, J. Seelig, Thermodynamics of the alpha-helix-coil transition of amphipathic peptides in a membrane environment: implications for the peptide-membrane binding equilibrium, J. Mol. Biol. 294 (1999) 785–794.
[41] T. Wieprecht, O. Apostolov, M. Beyermann, J. Seelig, Membrane binding and pore formation of the antibacterial peptide PGLa: thermodynamic and mechanistic aspects, Biochemistry 39 (2000) 442–452.
[42] T. Wieprecht, O. Apostolov, J. Seelig, Binding of the antibacterial peptide magainin 2 amide to small and large unilamellar vesicles, Biophys. Chem. 85 (2000) 187–198.
[43] P.R. Bergethon, E.R. Simons, Biophysical Chemistry: Molecules to Membranes, Springer Verlag, New York, 1990.
[44] S. Keller, I. Sauer, H. Strauss, K. Gast, M. Dathe, M. Bienert, Membrane-mimetic nanocarriers formed by a dipalmitoylated cell-penetrating peptide, Angew. Chem. Int. Ed. Engl. 44 (2005) 5252–5255.
[45] J. Seelig, 31P nuclear magnetic resonance and the head group structure of phospholipids in membranes, Biochim. Biophys. Acta 515 (1978) 105–140.
[46] S.C. Quay, C.C. Condie, Conformational studies of aqueous melittin: thermodynamic parameters of the monomer–tetramer self-association reaction, Biochemistry 22 (1983) 695–700.
[47] W. Wilcox, D. Eisenberg, Thermodynamics of melittin tetramerization determined by circular dichroism and implications for protein folding, Protein Sci. 1 (1992) 641–653.
[48] Y. Goto, Y. Hagihara, Mechanism of the conformational transition of melittin, Biochemistry 31 (1992) 732–738.
[49] S. Rex, G. Schwarz, Quantitative studies on the melittin-induced leakage mechanism of lipid vesicles, Biochemistry 37 (1998) 2336–2345.
[50] C. Mazzuca, B. Orioni, M. Coletta, F. Formaggio, C. Toniolo, G. Maulucci, M. De Spirito, B. Pispisa, M. Venanzi, L. Stella, Fluctuations and the rate-limiting step of peptide-induced membrane leakage, Biophys. J. 99 (2010) 1791–1800.
[51] R.M. Peitzsch, S. McLaughlin, Binding of acylated peptides and fatty acids to phospholipid vesicles: pertinence to myristoylated proteins, Biochemistry 32 (1993) 10436–10443.
[52] G.V. Richieri, R.T. Ogata, A.M. Kleinfeld, Thermodynamics of fatty acid binding to fatty acid-binding proteins and fatty acid partition between water and membranes measured using the fluorescent probe ADIFAB, J. Biol. Chem. 270 (1995) 15076–15084.